

PAPER • OPEN ACCESS

## Operando XRD studies on $\text{Bi}_2\text{MoO}_6$ as anode material for Na-ion batteries

To cite this article: Anders Brennhagen *et al* 2022 *Nanotechnology* **33** 185402

View the [article online](#) for updates and enhancements.

### You may also like

- [Simulation of the Kinetics of a Chemical System as a Method for Determination of Rate Constants from Experimental Data](#)  
Ole W Saastad and Einar Uggerud

- [The effect of fluoride surface modification of ceramic  \$\text{TiO}\_2\$  on the surface properties and biological response of osteoblastic cells \*in vitro\*](#)  
H Tiainen, M Monjo, J Knychala *et al.*

- [The doubly closed shell nucleus  \$^{132}\text{Sn}\$ : Collectivity and p-h states](#)  
B Fogelberg, M Hellström, D Jerrestam *et al.*



The Electrochemical Society  
Advancing solid state & electrochemical science & technology

242nd ECS Meeting

Oct 9 – 13, 2022 • Atlanta, GA, US

Abstract submission deadline: **April 8, 2022**

Connect. Engage. Champion. Empower. Accelerate.

**MOVE SCIENCE FORWARD**



Submit your abstract



# Operando XRD studies on $\text{Bi}_2\text{MoO}_6$ as anode material for Na-ion batteries

Anders Brennhagen<sup>1</sup> , Carmen Cavallo<sup>1,\*</sup> , David S. Wragg<sup>1,2</sup> ,  
Ponniiah Vajeeston<sup>1</sup> , Anja O. Sjøstad<sup>1</sup> , Alexey Y. Kopusov<sup>1,3</sup>  and  
Helmer Fjellvåg<sup>1,\*</sup> 

<sup>1</sup> Centre for Material Science and Nanotechnology, Department of Chemistry, University of Oslo, PO Box 1033, Blindern, N-0315, Oslo, Norway

<sup>2</sup> Norwegian National Resource Centre for x-ray Diffraction and Scattering (RECX), Department of Chemistry, University of Oslo, PO Box 1033, Blindern, N-0315, Oslo, Norway

<sup>3</sup> Department of Battery Technology, Institute for Energy Technology (IFE), Instituttveien 18, 2007, Kjeller, Norway

E-mail: [carmen.cavallo@smn.uio.no](mailto:carmen.cavallo@smn.uio.no) and [helmer.fjellvag@kjemi.uio.no](mailto:helmer.fjellvag@kjemi.uio.no)

Received 22 November 2021, revised 21 January 2022

Accepted for publication 25 January 2022

Published 10 February 2022



CrossMark

## Abstract

Based on the same rocking-chair principle as rechargeable Li-ion batteries, Na-ion batteries are promising solutions for energy storage benefiting from low-cost materials comprised of abundant elements. However, despite the mechanistic similarities, Na-ion batteries require a different set of active materials than Li-ion batteries. Bismuth molybdate ( $\text{Bi}_2\text{MoO}_6$ ) is a promising NIB anode material operating through a combined conversion/alloying mechanism. We report an *operando* x-ray diffraction (XRD) investigation of  $\text{Bi}_2\text{MoO}_6$ -based anodes over 34 (de)sodiation cycles revealing both basic operating mechanisms and potential pathways for capacity degradation. Irreversible conversion of  $\text{Bi}_2\text{MoO}_6$  to Bi nanoparticles occurs through the first sodiation, allowing Bi to reversibly alloy with Na forming the cubic  $\text{Na}_3\text{Bi}$  phase. Preliminary electrochemical evaluation in half-cells *versus* Na metal demonstrated specific capacities for  $\text{Bi}_2\text{MoO}_6$  to be close to  $300 \text{ mAh g}^{-1}$  during the initial 10 cycles, followed by a rapid capacity decay. *Operando* XRD characterisation revealed that the increased irreversibility of the sodiation reactions and the formation of hexagonal  $\text{Na}_3\text{Bi}$  are the main causes of the capacity loss. This is initiated by an increase in crystallite sizes of the Bi particles accompanied by structural changes in the electronically insulating Na–Mo–O matrix leading to poor conductivity in the electrode. The poor electronic conductivity of the matrix deactivates the  $\text{Na}_x\text{Bi}$  particles and prevents the formation of the solid electrolyte interface layer as shown by post-mortem scanning electron microscopy studies.

Supplementary material for this article is available [online](#)

Keywords: Na-ion batteries, SEI, PDF, Conversion-alloy anode materials, Post-mortem SEM, *Operando* XRD

(Some figures may appear in colour only in the online journal)

\* Authors to whom any correspondence should be addressed.



Original content from this work may be used under the terms of the [Creative Commons Attribution 4.0 licence](#). Any further distribution of this work must maintain attribution to the author(s) and the title of the work, journal citation and DOI.

## 1. Introduction

Li-ion batteries (LIBs) dominate the rechargeable battery market due to their high energy and power densities. However, Na-ion batteries (NIBs) have recently emerged as a promising alternative to LIBs due to the high abundance and low cost of Na [1, 2]. While there are many similarities

between LIBs and NIBs, some well-established LIB materials perform poorly for NIBs. Graphite as an anode material is a key example. The challenges associated with the use of graphite in NIBs led to a search for alternatives, where materials utilizing conversion and/or alloying reactions show promising performance [3]. Among those, Bi is a promising alloying anode material with a high theoretical capacity ( $385 \text{ mAh g}^{-1}$ ) and low operating potential ( $\sim 0.5 \text{ V}$ ) versus  $\text{Na}/\text{Na}^+$ . Unfortunately, like most alloying electrode materials, Bi suffers from poor cycling stability. Several strategies have been tested to stabilise the cycling behaviour of Bi. One of the most promising is the preparation of Bi-based materials that combine conversion and alloying in their cycling mechanisms. Bi-metallates, with a general formula of  $\text{Bi}_x\text{TM}_y\text{O}_z$  (TM = transition metal), are examples of these. Their operating mechanism consists of an irreversible conversion reaction during the first sodiation followed by reversible alloying of sodium ions with Bi formed in the initial conversion. The conversion reaction also appears to create a protective matrix around the Bi. The cycling stability of  $\text{BiVO}_4$  and  $\text{Bi}_2(\text{MoO}_4)_3$  is better than that of pure Bi [4, 5]. These materials show stable capacities of around  $350 \text{ mAh g}^{-1}$  for 100 cycles and 79% retained capacity after 1000 cycles [4]. Other Bi-metallates such as  $\text{BiFeO}_3$  [6] and  $\text{Bi}_2\text{MoO}_6$  [7] demonstrate capacities between 500 and  $600 \text{ mAh g}^{-1}$  during the first cycles, but stable long term cycling has not been achieved.

*Operando* x-ray absorption spectroscopy (XAS) and x-ray diffraction (XRD) investigations of the first 1.5 cycles of Bi-metallate NIB anodes suggest that the cycling mechanism involves the conversion of  $\text{Bi}_x\text{TM}_y\text{O}_z$  into small clusters of Bi metal and an amorphous Na-TM-O matrix during the first sodiation. The Bi then alloys reversibly with Na from pure Bi to  $\text{Na}_3\text{Bi}$ , while the Na-TM-O has low electrochemical activity [4].

Similar results are observed for Bi-metallate anodes in LIBs [8, 9], and the Bi to  $\text{Na}_3\text{Bi}$  cycling is also seen in NIBs with Bi metal [5, 10] and  $\text{Bi}_2\text{S}_3$  [11] anodes. The examples above, like most *operando* battery studies [12–15], only cover the first 1–2 cycles, however, significant structural changes that are crucial for long-term electrochemical performance can occur at later stages. In this work, we have performed an *operando* XRD evaluation of  $\text{Bi}_2\text{MoO}_6$  over 34 cycles, to obtain structural insight into both the cycling mechanisms and capacity degradation. This approach allows us to correlate cycling stability and capacity degradation with structural changes.

The solid electrolyte interface (SEI) on the anode surface in NIBs is believed to be crucial for cycling stability, and its instability contributes to capacity degradation. Ideally, it should be electrically insulating, have good ionic conductivity and be mechanically, electrochemically and thermally stable [16]. SEIs are complex and contain several different species that are highly dependent on the electrolyte, electrodes, binders and additives. The exact compositions remain uncertain, but  $\text{Na}_2\text{O}$ ,  $\text{Na}_2\text{CO}_3$  and NaF are often detected [17, 18]. Previous studies showed that the SEI formation in NIBs are

different from LIBs [19], where higher solubility of SEI components in NIB electrolytes is a big challenge [20].

By studying a large number of cycles *operando*, we confirm that the main cycling mechanism of  $\text{Bi}_2\text{MoO}_6$  is similar to the mechanism proposed in literature [4], but furthermore, initiate a discussion on what impacts the different phase changes have on capacity degradation. We also explore the formation and dissolution of the SEI layer on the  $\text{Bi}_2\text{MoO}_6$  surface as an alternative contributor to the capacity decay. By post-mortem scanning electron microscopy (SEM) studies, we observe the formation and dissolution of the SEI layer at different stages of cycling. The work provides a new perspective on the cycling mechanism of  $\text{Bi}_2\text{MoO}_6$  and, more generally, of conversion/alloying materials for Na-ion batteries.

## 2. Experimental

### 2.1. Materials

$\text{Bi}(\text{NO}_3)_3 \cdot 5\text{H}_2\text{O}$  (98%), ethylene glycol (99.8%), N-methyl-2-pyrrolidone (NMP) (99.5%), ethylene carbonate (EC) (99%), diethyl carbonate (DEC) (99%), fluoroethylene carbonate (FEC) (99%), sodium metal and sodium carboxymethylcellulose (CMC) were purchased from Sigma Aldrich and  $\text{Na}_2\text{MoO}_4 \cdot 2\text{H}_2\text{O}$  (99%) from Merck. We also bought Ethanol (99.7%) from VWR, Super P from Timical, Kynar polyvinylidene fluoride (PVDF) from Arkema, double-sided dendritic Cu foil (99.9%,  $10 \mu\text{m}$  thick) from Schlenk and  $\text{NaPF}_6$  from Fluorochem. The home laboratory production facility provided distilled  $\text{H}_2\text{O}$  (Resistivity  $> 1 \text{ M}\Omega \text{ cm}$ ). Na, FEC, DEC, EC and  $\text{NaPF}_6$  were stored in an Ar-filled glovebox (M-Braun,  $\text{H}_2\text{O}$  and  $\text{O}_2$  levels below 0.1 ppm) while ethylene glycol and NMP had protective caps. We used all the chemicals as purchased without any further purification or treatments, except when stated otherwise in the following sections.

### 2.2. Synthesis of $\text{Bi}_2\text{MoO}_6$

The synthesis is a modified procedure of a method previously reported in literature by Xin *et al* [7]. To synthesise  $\text{Bi}_2\text{MoO}_6$  we dissolved 1.26 g (5.2 mmol)  $\text{Na}_2\text{MoO}_4 \cdot 2\text{H}_2\text{O}$  and 5.06 g (10.4 mmol)  $\text{Bi}(\text{NO}_3)_3 \cdot 5\text{H}_2\text{O}$  in two separate beakers each with 15 ml of ethylene glycol under stirring for half an hour. Consecutively, the two solutions were mixed in a third container and 60 ml of ethanol was added dropwise followed by continuous stirring for an additional 1.5 h. Then we transferred the solution to a Teflon-lined stainless steel autoclave with an inner volume of 180 ml. The autoclave was heated in an oven at  $160 \text{ }^\circ\text{C}$  for 24 h and then naturally cooled down to room temperature. Finally, we obtained the  $\text{Bi}_2\text{MoO}_6$  microspheres by filtering, washing three times with ethanol and drying at  $60 \text{ }^\circ\text{C}$  in air. In the course of this work, we carried out several other solvothermal  $\text{Bi}_2\text{MoO}_6$  syntheses with different temperatures and heating times. The results of those syntheses and discussion of the structure, morphology and electrochemical performance of the products can be

found in section S1.1, S1.2 and figures S6-S12 (available online at [stacks.iop.org/NANO/33/185402/mmedia](https://stacks.iop.org/NANO/33/185402/mmedia)) in the supporting information (SI).

### 2.3. Material characterisation

X-ray diffraction (XRD) and pair distribution function (PDF) measurements on the pristine  $\text{Bi}_2\text{MoO}_6$  in a 0.7 mm borosilicate glass capillary were performed at beamline ID15A of the European Synchrotron (ESRF) in Grenoble. We used a Dectris Pilatus 3X 2M CdTe detector and monochromatic radiation with a wavelength of 0.1425 Å [21]. The 2D diffraction data were integrated with PyFai [22] and converted to PDFs with PDFgetX3 [23] after subtraction of a background measurement on an empty 0.7 mm borosilicate glass capillary. For pattern fitting of the XRD and PDF data, we used Topas v6 [24], while Vesta [25, 26] was utilized for visualization of the structure. We further investigated the morphology of the  $\text{Bi}_2\text{MoO}_6$  particles with a high-resolution Hitachi SU8230 cold-field emission scanning electron microscope (SEM), generating images using secondary electrons. We used an acceleration voltage of 5 kV, magnifications from 500 to 250,000 and a working distance of 8–10 mm. Carbon tape on the SEM holders ensured good conductivity and held the powder in place during the measurements.

### 2.4. Electrode preparation

For electrode preparation, we mixed 80 wt% active material ( $\text{Bi}_2\text{MoO}_6$ ) with 10 wt% Super P and 10 wt% PVDF binder in NMP in a Thinky® mixer (ARE 250). The slurry was cast on a 10 µm thick double-sided dendritic Cu foil using a motorised K control coater (RK) with a stainless steel doctor blade with the thickness set to 300 µm. After casting, we dried the electrodes (cut to 15 mm diameter, ~2 mg cm<sup>-2</sup> active material) overnight under ambient conditions in a fume hood followed by drying in a Buchi oven at 80 °C under dynamic vacuum for 4 h and then transferred to an Ar-filled glovebox (MBRAUN, H<sub>2</sub>O and O<sub>2</sub> levels below 0.1 ppm).

### 2.5. Electrochemical analysis

The electrochemical performance of the electrodes was tested in Na-ion half-cells, using Na metal as a counter electrode. We assembled coin cells using CR2032 stainless steel housings (304, Pi-Kem) with glass microfiber separators (17 mm, Whatman), soaked with 80 µl of electrolyte during cell assembly. The electrolyte was prepared in the glovebox with 1 M NaPF<sub>6</sub> in a 1:1 (volume ratio) mixture of EC and DEC with 5% FEC as additive. We prepared Na metal electrodes by removing the oxide layer from Na blocks (Sigma-Aldrich) with a scalpel, rolling them to form thin sheets (roughly 0.5 mm thick) and punching the discs with a diameter of 14 mm. An automatic coin cell crimper (Hohsen) pressed and sealed the cells. Galvanostatic cycling (GC) was performed using a battery tester (CT-4008T-5V10mA-164, Neware) with a voltage range of 0.01–2.00 V *versus* Na/Na<sup>+</sup>, specific current of 100 mA g<sup>-1</sup> and 12 h rest before cycling. For cyclic voltammetry (CV), we employed an MPG2 battery

cycler (BioLogic) with a voltage range of 0.01–2.00 V *versus* Na/Na<sup>+</sup> and a sweep rate of 0.1 mV s<sup>-1</sup>.

### 2.6. Electrode preparation for operando cell assembly and characterisation

For the *operando* XRD experiments, we used a laboratory manufactured cell similar to the one presented by Drozhzhin *et al* [27], with glassy carbon windows. The electrodes had CMC as a binder and distilled H<sub>2</sub>O as solvent. We added the slurry dropwise directly on the glassy carbon window (glued to the cathode half of the *operando* cell) with a glass pipette. The subsequent preparation steps were identical to the methodology described in section 2.3. The preparation procedure of the electrodes for the *operando* cells did not permit accurate determination of the active materials' mass. Therefore, the absolute, rather than specific, currents and capacities are presented for these measurements. We assembled the *operando* cells with Na metal as counter electrodes, glass fiber separator, 80 µl of 1 M NaPF<sub>6</sub> in EC:DEC (1:1) with 5% FEC as the electrolyte, and the studied electrode. GC measurements were performed with a current of 250 µA between 0.01 and 2.00 V using an SP150 battery cycler (BioLogic). We performed *operando* XRD measurements by continuous still scans (10 min scan<sup>-1</sup>, Q = 1.26–3.65 Å<sup>-1</sup>) with a D8 Advance diffractometer (Bruker, Mo source, λ = 0.7093) using a Dectris Eiger 2R detector in 1D mode.

### 2.7. Preparation of post-mortem samples for SEM

The electrodes and cells for post mortem SEM analysis were prepared as described in sections 2.3 and 2.4. The batteries cycled with a specific current of 100 mA g<sup>-1</sup> in the range of 0.01–2.00 V *versus* Na/Na<sup>+</sup>, except when stated otherwise in section 3.4 and figure 5. We stopped the measurement at certain stages of cycling as specified in section 3.4. To ensure that the ongoing electrochemical reactions at the given voltages were completed, we kept the voltage at the endpoint constant until the measured current was below 0.02 mA.

After disassembling the batteries with a coin cell disassembling tool (Hoshen) inside the glovebox, we carefully extracted the electrodes and cleaned them with 0.5 ml DEC. The drying process was carried out in the small glovebox antechamber under a dynamic vacuum. To minimize the air exposure, we mounted the electrodes to the sample holder inside the glovebox and transferred them into a glass container covered with parafilm and a latex glove to the SEM. The samples were exposed to air for less than 3 s during the transfer from the glass container to the SEM, which we expect to have minimal impact on their morphology.

## 3. Result and discussions

### 3.1. Structural and morphological characterisation

We characterised the as-synthesised  $\text{Bi}_2\text{MoO}_6$  sample by using XRD, PDF and SEM. Pattern fitting of the XRD and PDF measurements (figures 1(a) and (b)) confirmed that the sample

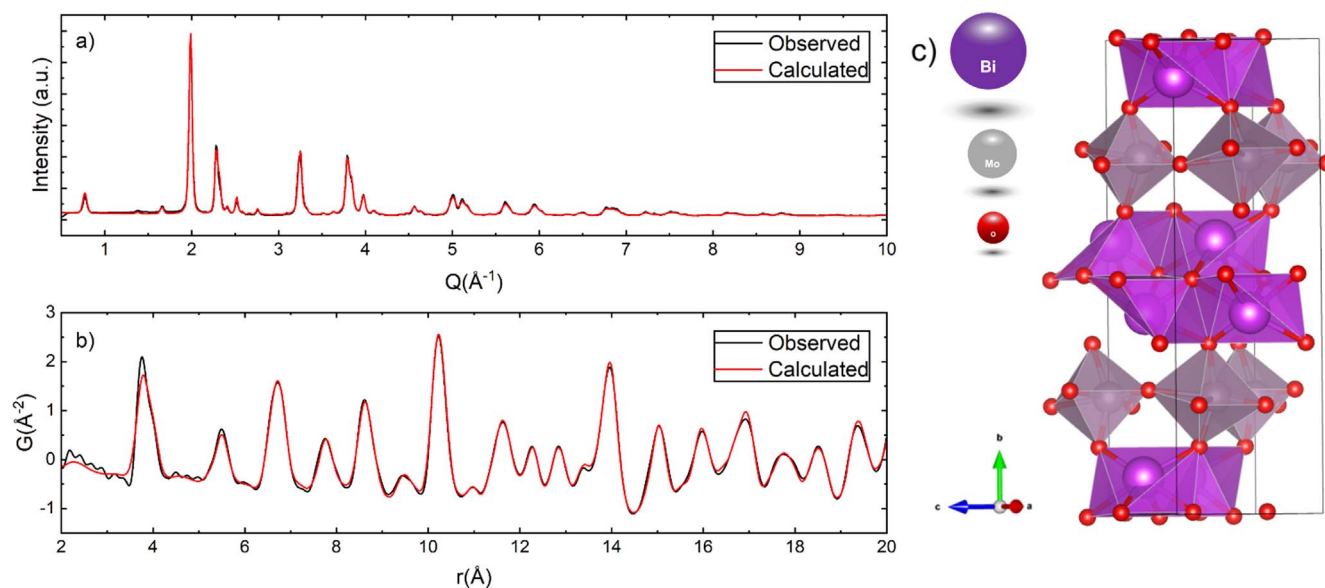


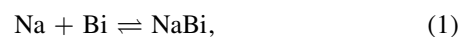
**Figure 1.** Pattern fitting of (a) XRD data and (b) PDF pattern of  $\text{Bi}_2\text{MoO}_6$  [28]. (c) visualization of the structure including coordination polyhedra where purple, grey and red spheres represent Bi, Mo and O atoms, respectively.

is phase-pure and composed of orthorhombic  $\text{Bi}_2\text{MoO}_6$  (spacegroup:  $\text{Pca}2_1$ ; COD ID: 1530868). The structure consists of layers of distorted Mo-O6 octahedra connected by corner-sharing (figure 1(c)). Bi atoms bond to six oxygen atoms and are organised in a double layer between the Mo layers. Table S1 (SI) provides more structural details. The SEM images of  $\text{Bi}_2\text{MoO}_6$  showed agglomerates of spherical particles with sizes between roughly 1–3  $\mu\text{m}$  (figures 2(a) and (b)). A more detailed analysis of the particles revealed the substructure comprised of nanoplatelets with an approximate thickness of 20 nm ordered in a ‘house-of-cards’ morphology (figures 2(c) and (d)). The 2D character of the nanoplatelets probably reflects the layered nature of the  $\text{Bi}_2\text{MoO}_6$  structure (figure 1(c)). Besides, the sample contained  $\sim 100$  nm thick spikes growing out of the particles (figure 2(d)). While the particle size, distribution of spikes and the size of the nanoplatelets varies through the sample, the thickness of the nanoplatelets is almost identical between the particles even when the microstructure differs (figure S1).

### 3.2. Electrochemical characterisation (sodiation and desodiation)

To investigate the electrochemical performance of  $\text{Bi}_2\text{MoO}_6$  we extracted selected sodiation-desodiation curves (figure 3(a)) and the corresponding  $dQ/dV$  plot (figure 3(b)) from a representative GC measurement. During the 1st sodiation, the material reached a specific capacity of  $650 \text{ mAh g}^{-1}$  (calculated from the mass of  $\text{Bi}_2\text{MoO}_6$ ) while during the 2nd sodiation only a capacity of  $350 \text{ mAh g}^{-1}$  was measured. This capacity loss is attributed to the irreversible *in situ* conversion of  $\text{Bi}_2\text{MoO}_6$  into Bi metal and a Mo-containing matrix as well as the formation of SEI layers. For cycles 2, 5 and 10, we observe 2 distinct plateaus (figure 3(a)) in the (de) sodiation curves and 2 peaks in the  $dQ/dV$  plot (figure 3(b))

corresponding to the following alloying reactions:



Reaction (1) corresponds to the  $dQ/dV$  peak at around 0.6 V during sodiation and 0.8 V during desodiation. Reaction (2) occurs around 0.4 V (sodiation) and 0.6 V (desodiation). This part of the reaction mechanism is similar to that of other Bi-metallates [4]. The theoretical capacity of reaction (1) and (2) combined is  $264 \text{ mAh g}^{-1}$ . This is significantly less than the observed specific capacity during the first 3 cycles, which is above  $300 \text{ mAh g}^{-1}$ . However, between cycles 3 and 10, the specific capacity is in the range of  $245\text{--}285 \text{ mAh g}^{-1}$  (both sodiation and desodiation), indicating that the observed capacity is almost exclusively derived from reactions (1) and (2). The origin of the extra capacity observed during the first 3 cycles is still uncertain, but redox reactions in the Mo-containing matrix may be involved. We evaluated the contribution of the conductive carbon additive, Super P, to the total capacity of the anode (section S2 and figure S13). It was approximately  $15 \text{ mAh g}^{-1}$ .

After 10 (de)sodiation cycles, the capacity of the  $\text{Bi}_2\text{MoO}_6$ -based electrodes exhibit a substantial decay (figure 3(c)). To elucidate the electrochemical changes occurring during this decay we extracted the (de)sodiation curves for cycles 9–14 (figure 3(d)). Inspection of those graphs clearly shows the complete disappearance of the plateaus corresponding to reaction (1), followed by a reduction of the second plateau corresponding to reaction (2).

Further tests were conducted on ball-milled  $\text{Bi}_2\text{MoO}_6$  to study the effect on cycling stability. As reported in sections S3.1, S3.2 and figures S14–S16, the materials did not perform better than the as-synthesised  $\text{Bi}_2\text{MoO}_6$ . We, therefore, proceeded with *operando* studies on the as-synthesised material only.

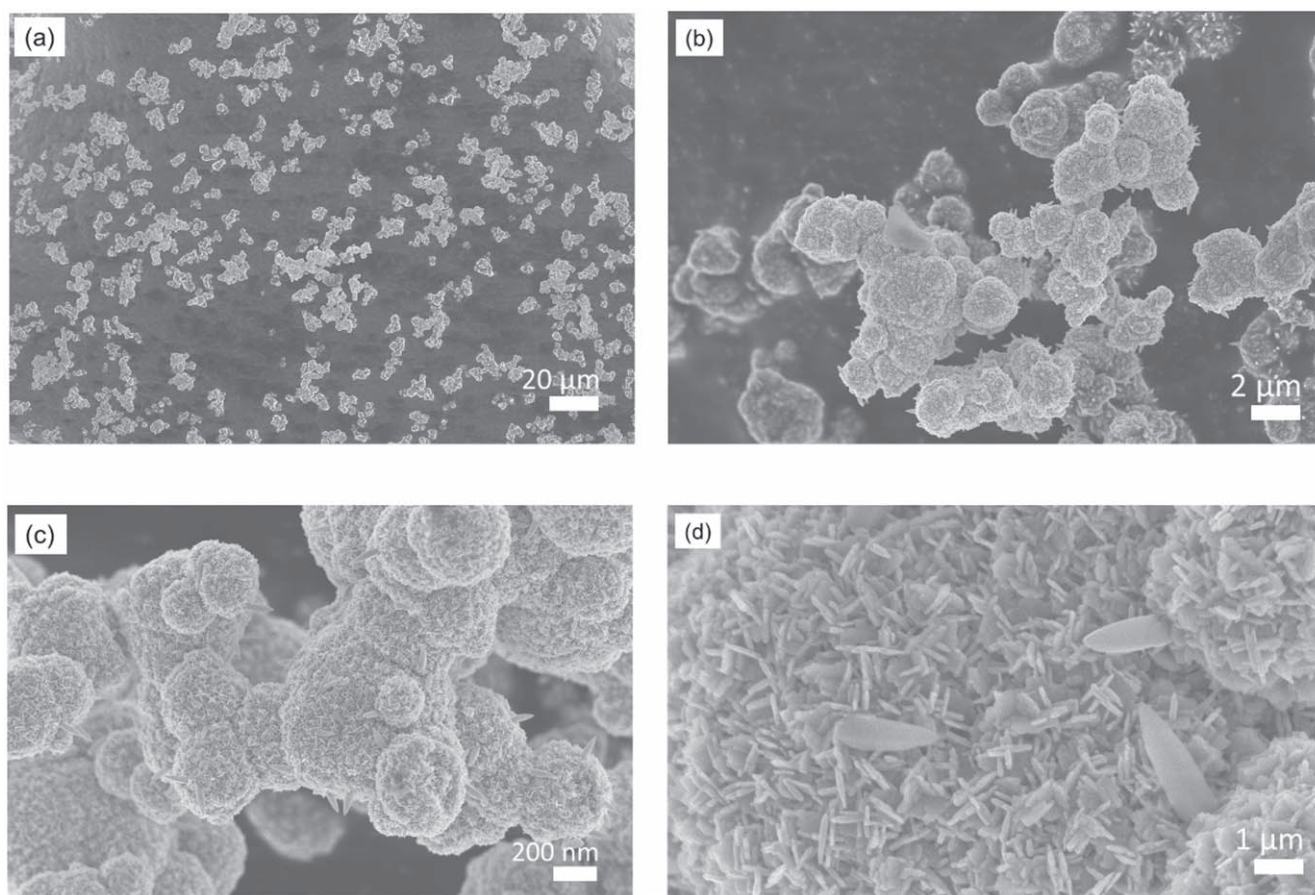


**Figure 2.** SEM images of the  $\text{Bi}_2\text{MoO}_6$  particles generated by secondary electrons at different magnifications: (a)  $\times 500$ , (b)  $\times 5000$ , (c)  $\times 10,000$  and (d)  $\times 50,000$ .

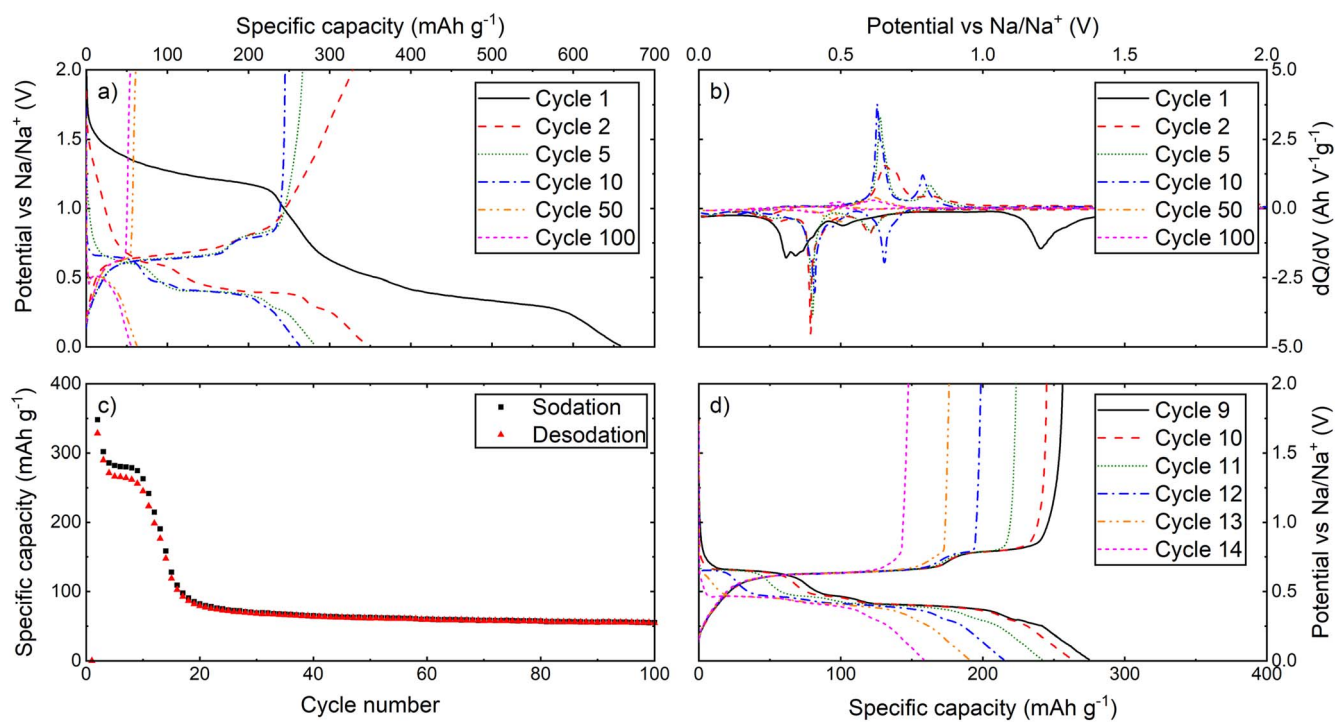


**Figure 3.** (a) (de)sodiation curves and (b) corresponding  $dQ/dV$  plot of selected cycles, (c) specific capacity over the first 100 cycles, (d) (de)sodiation curves of cycle 9–14 highlighting the region with rapid capacity decay. All graphs are derived from galvanostatic cycling (GC) measurements performed with a specific current of  $100 \text{ mA g}^{-1}$  with a voltage range of 0.01–2.00 V versus  $\text{Na}/\text{Na}^+$ .

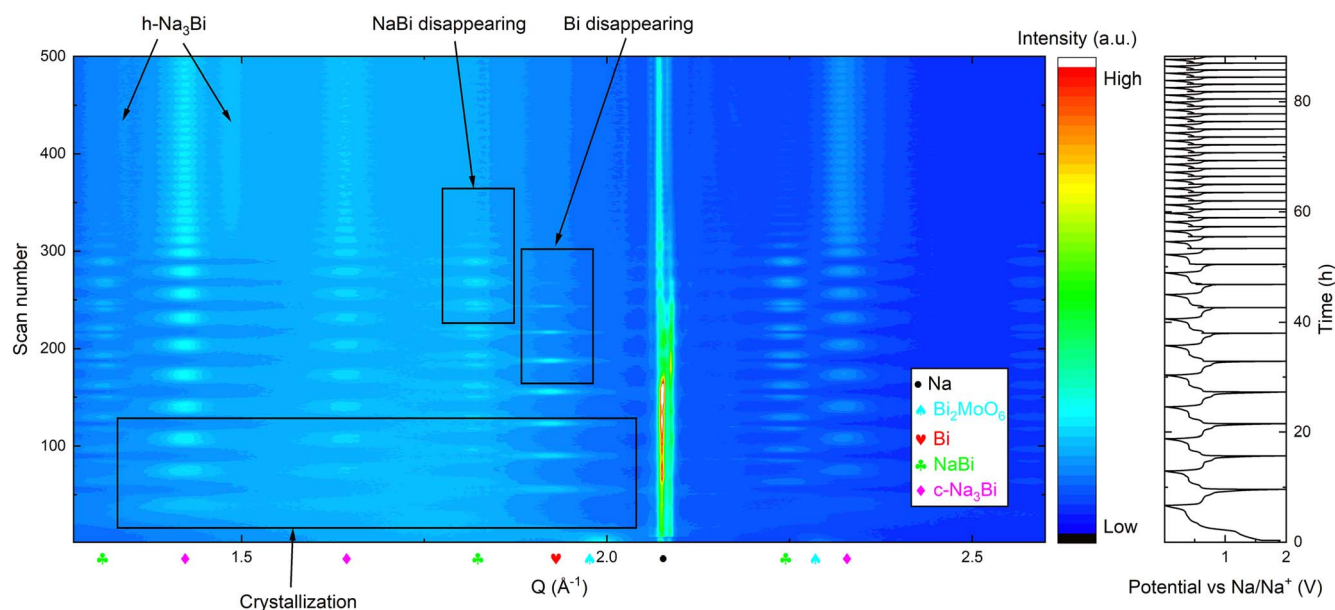


**Figure 4.** Operando XRD over 34 cycles of  $\text{Bi}_2\text{MoO}_6$  in Na half-cell obtained from GC measurements between 0.01–2.00 V versus  $\text{Na}/\text{Na}^+$  and a current of 250  $\mu\text{A}$ .

### 3.3. Cycling mechanism and capacity fade (operando XRD)

To further investigate the cycling mechanism of  $\text{Bi}_2\text{MoO}_6$  and understand the origin of capacity fading we performed operando XRD measurements over 34 cycles with GC (figure 4). The data in figure 4, and the extended contour plot in figure S4, unambiguously confirmed the main cycling reactions suggested in section 3.2:  $\text{Bi}_2\text{MoO}_6$  converts into Bi (COD: 2310889) at the start of the first sodiation. The Bi then reversibly alloys with Na to form NaBi (ICSD: 58816) and  $\text{Na}_3\text{Bi}$ . The  $\text{Na}_3\text{Bi}$  phase formed in the initial formation is the cubic phase of  $\text{Na}_3\text{Bi}$  (c- $\text{Na}_3\text{Bi}$ ) with the spacegroup Fm-3m and not the hexagonal phase (h- $\text{Na}_3\text{Bi}$ ) (COD: 1010291), which forms from microcrystalline Bi metal [5] (figure S5). Detailed information about the structures is reported in Table S1 (SI).

We also observe that the Bi peaks that appear during the first sodiation are significantly broader than those of the  $\text{Bi}_2\text{MoO}_6$  that disappear. Along with the observation of c- $\text{Na}_3\text{Bi}$ , this indicates that the Bi metal formed during the initial sodiation of  $\text{Bi}_2\text{MoO}_6$  is nanocrystalline. The operando data also provides insight into the chemical mechanism of degradation. During the first cycle, we observed that Bi, and the corresponding sodiated phases, are nanocrystalline. During the first 5 (de)sodiation cycles the peaks corresponding to Bi, NaBi and  $\text{Na}_3\text{Bi}$  gradually become sharper indicating an increase in the crystallite sizes. Around cycle 8, the diffraction peaks corresponding to metallic Bi gradually disappear. This corresponds to the start of the capacity decay. The exact point where the capacity decay starts may vary slightly between different cells; in the operando cell, the capacity decay begins a few cycles earlier than for the conventional coin cell described in section 3.2. The disappearance of the Bi XRD peaks together with the disappearance of the Bi–NaBi plateau in the (de)sodiation curves confirms that reaction (1)

gradually becomes irreversible and Bi is no longer formed during desodiation after cycle 8. Over the next few cycles, similar irreversibility occurs for reaction (2) as more and more NaBi converts into  $\text{Na}_3\text{Bi}$  during sodiation but is not recovered during desodiation. That process is accompanied by the formation of the h- $\text{Na}_3\text{Bi}$  phase in addition to c- $\text{Na}_3\text{Bi}$ . The appearance of h- $\text{Na}_3\text{Bi}$  could be explained by the increased crystallite size of active domains, as Sottmann *et al* showed for Bi metal [5]. The same study also showed that the h- $\text{Na}_3\text{Bi}$  has poor cycling stability compared to the cubic phase, due to a structural mismatch with NaBi. Our results suggest that for  $\text{Bi}_2\text{MoO}_6$  the reversibility of cycling to/from c- $\text{Na}_3\text{Bi}$  is also greatly reduced in later cycles, as the corresponding diffraction peaks vary only slightly in intensity and do not disappear during desodiation. Therefore, we believe that the mechanism of capacity decay is primarily driven by the Mo-containing matrix formed during the initial sodiation, rather than by the formation of large h- $\text{Na}_3\text{Bi}$  crystallites.

The operando XRD data provided full insight into the crystalline phases formed throughout the cycle life of our battery, however, it does not reveal information regarding the amorphous phases. There is no sign of Mo-containing phases in the observed diffractograms, confirming its amorphous nature after the first sodiation. During the crystal growth of the Bi particles, it is likely that structural changes happen to the Na–Mo–O matrix. A set of Na–Mo–O compounds was previously screened by ‘The Materials Project’ [29], showing that all of them are electronic insulators. Therefore, it is reasonable to assume that structural transformations that take place during cycling result in a thicker matrix of Na–Mo–O around Bi, NaBi and  $\text{Na}_3\text{Bi}$  sub-particles, inhibiting the desodiation process. We will, in future studies, investigate this aspect with techniques like PDF and extended x-ray absorption fine structure (EXAFS) that are sensitive to amorphous phases.

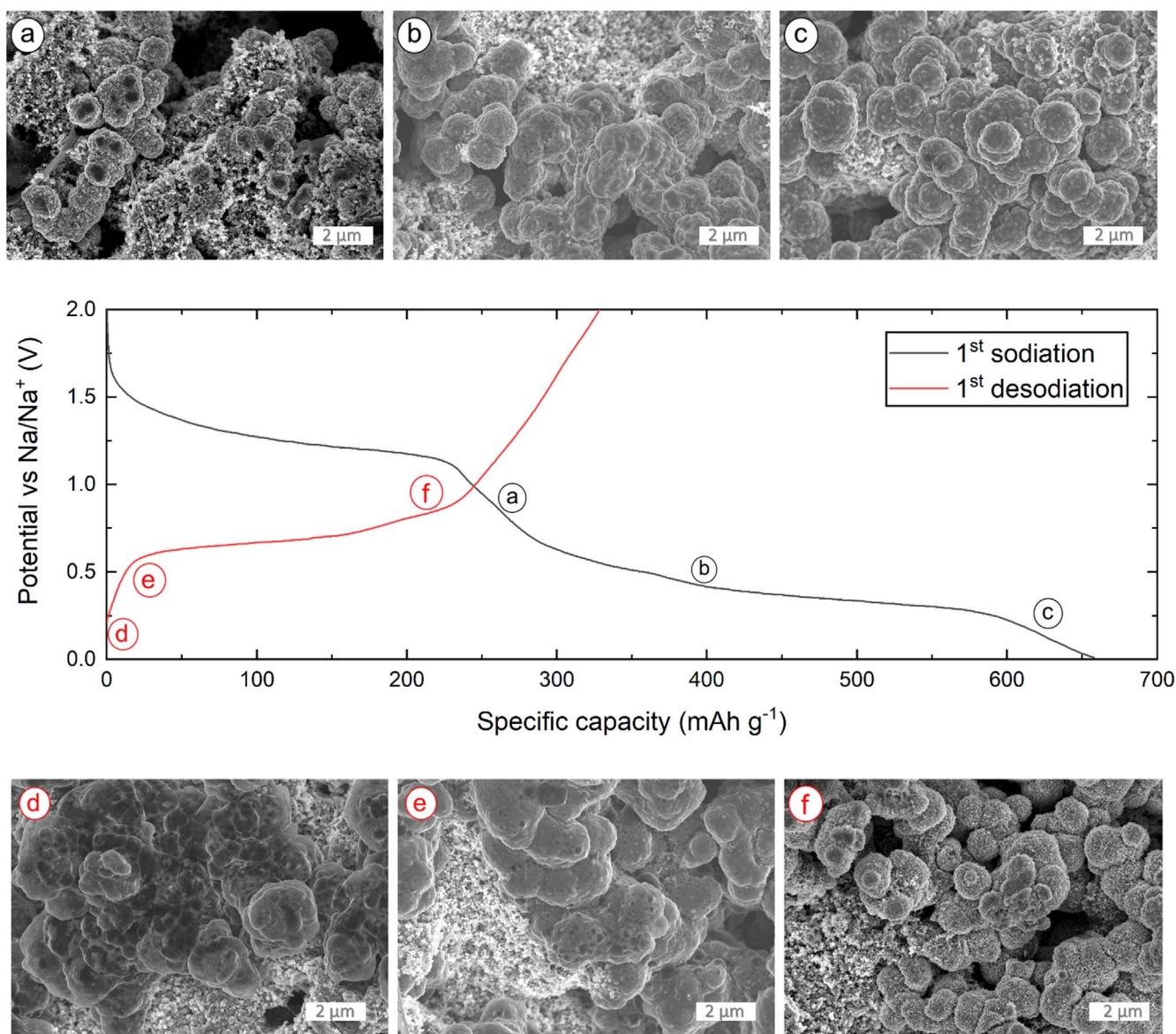


**Figure 5.** Post-mortem SEM images captured with a secondary electron detector at different sodiation states during the first cycle. (a) sodiated to 1.00 V, (b) sodiated to 0.50 V, (c) sodiated to 0.35 V, (d) fully sodiated to 0.01 V, (e) desodiated to 0.50 V and (f) desodiated to 0.90 V *versus* Na/Na<sup>+</sup>.

### 3.4. Post-mortem SEM

Dissolution of the SEI is a common problem for NIB anode materials [20]. To study the SEI formation, we performed post-mortem SEM on electrodes extracted at different states of charge (figure 5). During the 1<sup>st</sup> sodiation, the SEI layer starts to form already above 1 V *versus* Na/Na<sup>+</sup>, visible as dark spots in figure 5(a). However, the SEI only covers a few areas of the electrode surface at this stage of cycling. At 0.50 and 0.35 V, the particles are completely covered, as they have a smooth surface showing no characteristic signs of the nanoplatelets from the pristine material (figures 5(b) and (c)). This confirms that the formation of the SEI layer mostly occurs between 1.00 and 0.50 V during the 1<sup>st</sup> sodiation. During the 1<sup>st</sup> desodiation, the SEI layer is still intact at 0.50 V, but it is not present above 0.90 V as the nanoplatelets are again observed (figure 5(d)). This means that the SEI layer

forms and dissolves in the same voltage range as the alloying reactions between Na and Bi occur. Hence, we are unable to avoid the formation and dissolution of the SEI layer with our current electrolyte composition. To determine the role of the SEI on cycling stability, we extracted desodiated (2.00 V) and sodiated (0.01 V) samples at different stages of cycling. There is clearly an SEI forming on the surface of the particles in the samples imaged after the 1<sup>st</sup>, 2<sup>nd</sup> and 10<sup>th</sup> sodiation (figures S2(a), (b) and (c), respectively). After the 1<sup>st</sup> sodiation, the particles are quite uniformly coated as the main particle shapes are still visible, as opposed to the 2<sup>nd</sup> sodiation where the SEI covers whole agglomerates. After the 10<sup>th</sup> sodiation, the particle shapes become more visible again as the SEI layer becomes thinner and covers less of the surface. There are also certain areas where particles without a visible SEI layer are present. After the 20<sup>th</sup> sodiation (figure S2d, SI) the SEI layer is almost completely gone.



When studying the desodiated samples from the corresponding cycles (figure S3, SI) it is evident that the SEI layer disappears during the desodiation process. This indicates that the SEI layer is formed in every sodiation and dissolved in every desodiation during at least the first 10 cycles. This reaction consumes Na ions and may explain why the sodiation capacity is higher than the desodiation capacity during the first 10 cycles (figure 3(c)). When the SEI layer struggles to reform after 10 cycles it is reasonable to assume that this process is linked to the capacity decay observed between cycles 10 and 20. One theory we considered is that the repeated formation and dissolution of the SEI consumes vital components in the electrolyte during the first 10 cycles. When these components are depleted, the SEI no longer forms possibly leading to the structural changes observed in the *operando* XRD and the capacity decay. However, electrochemical measurements performed on Bi<sub>2</sub>MoO<sub>6</sub> samples (section S4, figure S17, SI) with different amounts of electrolyte indicates that the rapid loss of electrochemical performance does not depend on the amount of the electrolyte used. Even in a cell where we replaced both the electrolyte and the Na counter electrode after 10 cycles, the decay in capacity continued in the same fashion. The capacity decay does not, therefore, originate from the consumption of critical electrolyte components. The structural changes discussed in section 3.3 thus appear to be the main cause of both the capacity degradation and the changes in SEI formation.

A common degradation mechanism for alloying materials is particle fracturing and pulverization caused by large volume changes during cycling [30–33]. From the SEM images in this study (figure 5, S2 and S3), we do not observe any signs of cracking. We believe this is due to the protective effect of the Na-TM-O matrix, which mitigates the strain caused by the volume changes.

During the SEM study, we also observed an increasing amount of charging effects, with cycle number, leading to dark stripes in the images (figure S3(d)), which indicates poor electronic conductivity. This is also supported by electrochemical impedance spectroscopy measurements performed on the cells after the 1st and 20th desodiation, where the last cell showed much higher impedance (section S5, figure S18). This poor conductivity is most likely the leading cause of the capacity decay and can explain why the SEI layer no longer forms during the 20th sodiation. The question of exactly which structural changes in the material lead to this poor conductivity needs to be addressed in future studies.

#### 4. Conclusions and perspectives

Bi<sub>2</sub>MoO<sub>6</sub> is a potentially promising anode material for NIBs but requires further studies with appropriate nanostructuring and carbon additives to enhance the electronic conductivity. We have yet to find the perfect approach to ensure a long cycle life. However, by using *operando* XRD over a large number of cycles and post-mortem SEM, we have elucidated the cycling and degradation mechanism in this material and possibly a general trend in Bi-metallates as anode materials

for Na-ion batteries. The reversible cycling between Bi and c-Na<sub>3</sub>Bi through NaBi is the main cycling mechanism for the 10 first cycles, where the capacity is stable and close to 300 mAh g<sup>-1</sup>. Following this, a rapid capacity decay occurs as the Bi-NaBi and NaBi-Na<sub>3</sub>Bi reactions become more irreversible followed by the formation of h-Na<sub>3</sub>Bi. At the same stage of cycling the SEI layer stops forming during sodiation. We postulate that the sudden onset of capacity loss is driven by structural changes, crystallite growth in the Na<sub>x</sub>Bi particles and growth of a thick, insulating Na-Mo-O matrix, with the disappearance of the SEI being a symptom of these rather than the cause of capacity loss.

Future studies on the structure and electrochemical properties of the amorphous Na-Mo-O will further improve our understanding of the cycling and degradation mechanisms of Bi<sub>2</sub>MoO<sub>6</sub>, and help to find an approach that could improve the cycling stability of this and similar materials.



#### Acknowledgments

This work was performed with support from the Research Council of Norway (NFR) through the NanoName project (number 287480). We acknowledge the use of the Norwegian national infrastructure for x-ray diffraction and Scattering (RECX) where we performed all our *operando* measurements. We acknowledge the European Synchrotron Radiation Facility (ESRF) for the provision of beamtime on ID15A and we would like to thank Stefano Checchia for the support during our beam time.

#### Data availability statement

All data that support the findings of this study are included within the article (and any supplementary files).

#### ORCID iDs

Anders Brennhagen  <https://orcid.org/0000-0003-4467-6750>  
Carmen Cavallo  <https://orcid.org/0000-0003-1931-3018>  
David S. Wragg  <https://orcid.org/0000-0001-8502-7912>  
Ponniiah Vajeeston  <https://orcid.org/0000-0002-5566-2429>  
Anja O. Sjøstad  <https://orcid.org/0000-0001-9280-541X>  
Alexey Y. Kuposov  <https://orcid.org/0000-0001-5898-3204>  
Helmer Fjellvåg  <https://orcid.org/0000-0001-6045-7211>

#### References

- [1] Hasa I *et al* 2021 Challenges of today for Na-based batteries of the future: from materials to cell metrics *J. Power Sources* **482** 228872
- [2] Vaalma C, Buchholz D, Weil M and Passerini S 2018 A cost and resource analysis of sodium-ion batteries *Nat. Rev. Mater.* **3** 18013

- [3] Zhang H, Hasa I and Passerini S 2018 Beyond insertion for na-ion batteries: nanostructured alloying and conversion anode materials *Adv. Energy Mater.* **8** 1702582
- [4] Sottmann J et al 2017 Bismuth vanadate and molybdate: stable alloying anodes for sodium-ion batteries *Chem. Mater.* **29** 2803–10
- [5] Sottmann J et al 2016 How crystallite size controls the reaction path in nonaqueous metal ion batteries: the example of sodium bismuth alloying *Chem. Mater.* **28** 2750–6
- [6] Xia H, Yan F, Lai M O, Lu L and Song W 2009 Electrochemical properties of BiFeO<sub>3</sub> thin films prepared by pulsed laser deposition *Funct. Mater. Lett.* **2** 163–7
- [7] Xu X, Li M and Yu T 2020 Facile synthesis of Bi<sub>2</sub>MoO<sub>6</sub> nanosheets@nitrogen and sulfur codoped graphene composites for sodium-ion batteries *Chem. Res. Chin. Univ.* **36** 115–9
- [8] Ruud A, Sottmann J, Vajeeston P and Fjellvåg H 2018 Operando investigations of lithiation and delithiation processes in a BiVO<sub>4</sub> anode material *Phys. Chem. Chem. Phys.* **20** 29798–803
- [9] Ruud A, Sottmann J, Vajeeston P and Fjellvåg H 2019 Direct observation of reversible conversion and alloying reactions in a Bi<sub>2</sub>(MoO<sub>4</sub>)<sub>3</sub>-based lithium-ion battery anode *J. Mater. Chem. A* **7** 17906–13
- [10] Gao H et al 2018 Sodium storage mechanisms of bismuth in sodium ion batteries: An operando x-ray diffraction study *J. Power Sources* **379** 1–9
- [11] Sottmann J, Homs-Regojo R, Wragg D S, Fjellvåg H, Margadonna S and Emerich H 2016 Versatile electrochemical cell for Li/Na-ion batteries and high-throughput setup for combined operando x-ray diffraction and absorption spectroscopy *J. Appl. Crystallogr.* **49** 1972–81
- [12] Liu D et al 2019 Review of recent development of *in situ* /operando characterization techniques for lithium battery research *Adv. Mater.* **31** 1806620
- [13] Zhang G et al 2017 Electrochemical *in situ* x-ray probing in lithium-ion and sodium-ion batteries *J. Mater. Sci.* **52** 3697–718
- [14] Zhu W et al 2018 Application of operando x-ray diffractometry in various aspects of the investigations of lithium/sodium-ion batteries *Energies* **11** 2963
- [15] Brennhagen A, Cavallo C, Wragg D S, Sottmann J, Kuposov A Y and Fjellvåg H 2021 Understanding the (De) Sodiation mechanisms in na-based batteries through operando x-ray methods *Batteries Supercaps* **4** 1039–63
- [16] Huang Y, Zhao L, Li L, Xie M, Wu F and Chen R 2019 Electrolytes and electrolyte/electrode interfaces in sodium-ion batteries: from scientific research to practical application *Adv. Mater.* **31** 1808393
- [17] Bommier C and Ji X 2018 Electrolytes, SEI formation, and binders: a review of nonelectrode factors for sodium-ion battery anodes *Small* **14** 1703576
- [18] Fondard J, Irisarri E, Courrèges C, Palacin M R, Ponrouch A and Dedryvère R 2020 SEI composition on hard carbon in na-ion batteries after long cycling: influence of salts (NaPF<sub>6</sub>, NaTFSI) and additives (FEC, DMCF) *J. Electrochem. Soc.* **167** 070526
- [19] Philippe B, Valvo M, Lindgren F, Rensmo H and Edström K 2014 Investigation of the electrode/electrolyte interface of Fe<sub>2</sub>O<sub>3</sub> composite electrodes: li versus na batteries *Chem. Mater.* **26** 5028–41
- [20] Ma L A, Naylor A J, Nyholm L and Younesi R 2021 Strategies for mitigating dissolution of solid electrolyte interphases in sodium-ion batteries *Angew. Chem.* **133** 4905–13
- [21] Vaughan G B M et al 2020 ID15A at the ESRF—a beamline for high-speed operando x-ray diffraction, diffraction tomography and total scattering *Journal of Synchrotron Radiation* **27** 515–28
- [22] Ashiotis G et al 2015 The fast azimuthal integration Python library: pyFAI *Journal of Applied Crystallography* **48** 510–9
- [23] Juhás P, Davis T, Farrow C L and Billinge S J L 2013 PDFgetX3: a rapid and highly automatable program for processing powder diffraction data into total scattering pair distribution functions *Journal of Applied Crystallography* **46** 560–6
- [24] Coelho A A and IUCr 2018 TOPAS and TOPAS-Academic: an optimization program integrating computer algebra and crystallographic objects written in C++ *Journal of Applied Crystallography* **51** 210–8
- [25] Momma K and Izumi F 2008 VESTA: a three-dimensional visualization system for electronic and structural analysis *Journal of Applied Crystallography* **41** 653–8
- [26] Momma K and Izumi F 2011 VESTA 3 for three-dimensional visualization of crystal, volumetric and morphology data *Journal of Applied Crystallography* **44** 1272–6
- [27] Drozhzhin O A, Tereshchenko I V, Emerich H, Antipov E V, Abakumov A M and Chernyshov D 2018 An electrochemical cell with sapphire windows for operando synchrotron x-ray powder diffraction and spectroscopy studies of high-power and high-voltage electrodes for metal-ion batteries *J. Synchrotron Radiat.* **25** 468–72
- [28] Wragg D, Brennhagen A, Villeveille C and Checchia S 2021 Modulation enhanced operando pdf for battery materials *European Synchrotron Radiation Facility (ESRF)* (<https://doi.org/10.15151/ESRF-ES-433977821>)
- [29] Jain A et al 2013 Commentary: the materials project: a materials genome approach to accelerating materials innovation *APL Mater.* **1** 011002
- [30] Lao M, Zhang Y, Luo W, Yan Q, Sun W and Dou S X 2017 Alloy-based anode materials toward advanced sodium-ion batteries *Adv. Mater.* **29** 1700622
- [31] Liu X H, Zhong L, Huang S, Mao S X, Zhu T and Huang J Y 2012 Size-dependent fracture of silicon nanoparticles during lithiation *ACS Nano* **6** 1522–31
- [32] Ulvestad A et al 2021 Stoichiometry-controlled reversible lithiation capacity in nanostructured silicon nitrides enabled by *in situ* conversion reaction *ACS Nano* **15** 16777–87
- [33] Wang J, Eng C, Chen-Wiegart Y K and Wang J 2015 Probing three-dimensional sodiation–desodiation equilibrium in sodium-ion batteries by *in situ* hard x-ray nanotomography *Nat. Commun.* **6** 1–9